2017

Evolutionary fine-tuning of conformational ensembles in FimH during host-pathogen interactions

Vasilios Kalas
Washington University School of Medicine in St. Louis

Jerome S. Pinkner
Washington University School of Medicine in St. Louis

Thomas J. Hannan
Washington University School of Medicine in St. Louis

Michael E. Hibbing
Washington University School of Medicine in St. Louis

Karen W. Dodson
Washington University School of Medicine in St. Louis

See next page for additional authors

BIOMOLECULES

Evolutionary fine-tuning of conformational ensembles in FimH during host-pathogen interactions

Vasilios Kalas,[1,2,3] Jerome S. Pinkner,[1,2] Thomas J. Hannan,[1,2,4] Michael E. Hibbing,[1,2] Karen W. Dodson,[1,2] Alex S. Holehouse,[3,5] Hao Zhang,[6] Niraj H. Tolia,[2] Michael L. Gross,[6] Rohit V. Pappu,[3,5] James Janetka,[6] Scott J. Hultgren[1,2]*

Positive selection in the two-domain type 1 pilus adhesin FimH enhances *Escherichia coli* fitness in urinary tract infection (UTI). We report a comprehensive atomic-level view of FimH in two-state conformational ensembles in solution, composed of one low-affinity tense (T) and multiple high-affinity relaxed (R) conformations. Positively selected residues allosterically modulate the equilibrium between these two conformational states, each of which engages mannose through distinct binding orientations. A FimH variant that only adopts the R state is severely attenuated early in a mouse model of uncomplicated UTI but is proficient at colonizing catheterized bladders in vivo or bladder transitional-like epithelial cells in vitro. Thus, the bladder habitat has barrier(s) to R state–mediated colonization possibly conferred by the terminally differentiated bladder epithelium and/or decoy receptors in urine. Together, our studies reveal the conformational landscape in solution, binding mechanisms, and adhesive strength of an allosteric two-domain adhesin that evolved "moderate" affinity to optimize persistence in the bladder during UTI.

INTRODUCTION

Bacterial pathogens adhere to and establish footholds in favorable habitats within their host. Adhesion often confers fitness advantages to bacterial pathogens by promoting access to essential nutrients, resistance to displacement by fluid flow, or evasion of immune responses (*1*–*3*). Bacterial pathogens have evolved numerous ways in which to achieve adhesion either specifically or nonspecifically through extracellular structures that include capsules, extracellular polymeric substances, pili/fimbriae, flagella, and other diverse adhesins (*1*, *4*, *5*). Many of these adhesive virulence mechanisms figure prominently in the colonization of the bladder by uropathogenic *Escherichia coli* (UPEC), which account for approximately 85% of all urinary tract infections (UTIs) (*6*, *7*). Mouse models have shown that adhesive hair-like surface appendages called type 1 pili allow UPEC to colonize the bladder epithelium during UTIs by binding to mannosylated receptors on the urothelial surface through the tip-localized adhesin FimH (*8*). Clinical observations and mouse models of UTI have shown that FimH mediates the invasion of UPEC into bladder superficial umbrella cells via endocytosis (*9*–*12*). Escape from the endocytic vesicle allows UPEC to replicate within the cytosol to form intracellular bacterial communities (IBCs), which is one mechanism used by UPEC to subvert neutrophil attack, thus facilitating survival and dissemination during UTI (*9*–*12*).

Consistent with its vital role in bacterial colonization of the bladder, FimH has evolved within human uropathogenic strains of *E. coli* by positive selection (*13*). FimH is composed of the following: (i) an N-terminal lectin domain ($FimH_{LD}$) that binds mannose via a pocket formed by three loops, (ii) a C-terminal pilin domain ($FimH_{PD}$) that noncovalently joins FimH to the pilus tip, and (iii) a five–amino acid linker that connects the two domains (Fig. 1A). It has been shown that three positively selected residues (residues 27, 62, and 163), which lie outside the mannose-binding pocket, modulate conformational changes in FimH (Fig. 1B) (*14*). Crystal structures of FimH in various stages of pilus assembly have revealed that $FimH_{PD}$ exists in one conformation but $FimH_{LD}$ has at least two conformational states that show distinct affinities for mannose (Fig. 1B) (*15*–*19*). Before pilus assembly, the incomplete immunoglobulin (Ig)–like fold of $FimH_{PD}$ is stabilized via a donor strand complementation interaction with the chaperone FimC in the periplasm (*15*, *20*). Crystal structures have revealed that FimH adopts an elongated conformation when bound to FimC, wherein $FimH_{LD}$ and $FimH_{PD}$ do not interact with each other and $FimH_{LD}$ is in a high-affinity mannose-binding state. Thereafter, the FimC-FimH (FimCH) complex initiates pilus assembly at the outer membrane, where the FimD usher catalyzes donor strand exchange (DSE), in which the N-terminal extension (Nte) of FimG displaces FimC to complete the Ig-like fold of $FimH_{PD}$ (*21*–*23*). Crystal structures show that FimH adopts a compact conformation when bound to FimG, wherein $FimH_{LD}$ and $FimH_{PD}$ interact closely with one another and $FimH_{LD}$ adopts a low-affinity mannose-binding state. To succinctly describe the correlation between all the structural and functional properties of FimH in its two known conformations (Fig. 1B), we adapted the nomenclature used in the Monod-Wyman-Changeux model of allostery to herein refer to the high-affinity conformation as the relaxed (**R**) state and the low-affinity conformation as the tense (**T**) state. On the basis of these structures, an allosteric model that links the conformation of FimH to its mannose-binding function has been proposed (Fig. 1C) (*17*, *24*). This model posits that $FimH_{PD}$ can allosterically diminish the ability of $FimH_{LD}$ to bind mannose through interactions with the base of $FimH_{LD}$. Conversely, mannose binding to $FimH_{LD}$ appears to promote $FimH_{LD}$ conformations that no longer interact with $FimH_{PD}$. However, the structural and evolutionary basis for conformational allostery in FimH at the pilus tip remains incompletely understood. Here, we characterize the conformational ensembles, dynamics, and binding mechanisms of FimH variants in a tip-like setting in solution. We discovered a mechanism whereby positively

[1]Center for Women's Infectious Disease Research, Department of Molecular Microbiology, Washington University School of Medicine, St. Louis, MO 63110, USA. [2]Department of Molecular Microbiology, Washington University School of Medicine, St. Louis, MO 63110, USA. [3]Department of Biochemistry and Molecular Biophysics, Washington University School of Medicine, St. Louis, MO 63110, USA. [4]Department of Pathology and Immunology, Washington University School of Medicine, St. Louis, MO 63110, USA. [5]Department of Biomedical Engineering and Center for Biological Systems Engineering, Washington University in St. Louis, St. Louis, MO 63130, USA. [6]Department of Chemistry, Washington University in St. Louis, St. Louis, MO 63130, USA.
*Corresponding author. Email: hultgren@wustl.edu

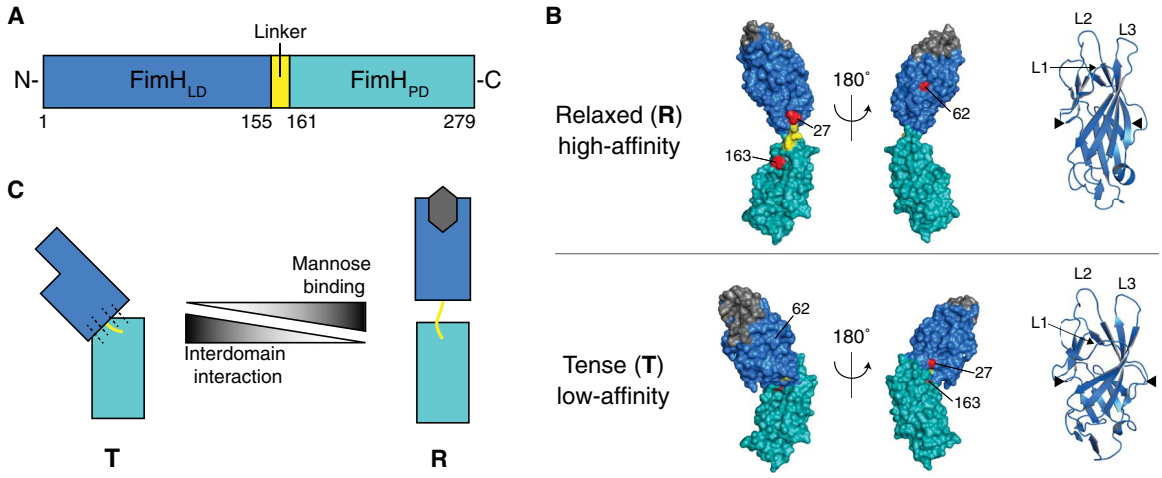

Fig. 1. Structure-function relationship in the type 1 adhesin FimH. (**A**) Schematic representation of FimH sequence. The lectin domain ($FimH_{LD}$, residues 1 to 155) is colored blue, the linker is colored yellow (residues 156 to 160), and the pilin domain ($FimH_{PD}$, residues 161 to 279) is colored teal. (**B**) Comparison of previously identified conformations of FimH. FimH bound to FimC in a FimCH complex exists in a high-affinity conformer, or **R** state, with an elongated orientation between $FimH_{LD}$ and $FimH_{PD}$, a narrowly packed β-sandwich fold in $FimH_{LD}$ (as highlighted between the two black triangles), and packed mannose-binding loops (labeled as L1, L2, and L3). FimH in a tip assembly (FimCFFGH complex) adopts a low-affinity conformer, or **T** state, with a compacted orientation between $FimH_{LD}$ and $FimH_{PD}$, a widened β-sandwich fold in $FimH_{LD}$ (as highlighted between the two black triangles), and displaced binding loops (particularly L1). Positively selected residues are indicated as red spheres, and the mannose-binding pocket is shaded gray. (**C**) Schematic representation of the negatively coupled allosteric relationship between mannose and the interface between FimH domains, whereby increases in mannose binding disfavor contacts between $FimH_{LD}$ and $FimH_{PD}$ and vice versa.

selected residues allosterically modulate a two-state conformational equilibrium in FimH to adapt a "moderate" mannose-binding affinity for optimal colonization of the bladder during UTI.

RESULTS

$FimG_{Nte}H$ functions as a type 1 pilus tip-like setting

Biophysical experiments to directly probe conformations of FimH within an in vitro reconstituted pilus tip have remained challenging because of the inherent tendency of pilus subunits, or pilins, to self-polymerize and introduce heterogeneity in solution (*14*). Thus, we created a "minimal" tip-like FimH complex through a spontaneous in vitro DSE reaction between FimH and a peptide corresponding to the Nte of FimG ($FimG_{Nte}$, residues 1 to 15) (Fig. 2A). This strategy was based on previous work that demonstrated how Nte peptides stabilize pilin domains (*22*). We investigated the conformational and functional effects of allelic variation in positively selected residues A27, A62, and V163 (*13*, *14*) on FimH within the $FimG_{Nte}H$ complex. This was done using the FimH sequence of the UPEC strain UTI89 (*25*) as the wild-type (WT) background. We produced $FimG_{Nte}H$ complexes with WT and variant FimH sequences (A62S, A27V/V163A) and the Q133K variant, a binding pocket mutation that abrogates adhesion (*13*). As with other DSE interactions (*14*), all purified $FimG_{Nte}H$ complexes exhibited high stability because all FimH variants remained bound to $FimG_{Nte}$ in the SDS sample buffer at room temperature (~31 kDa) but dissociated when boiled (~29 kDa) (Fig. 2B). Moreover, these variant $FimG_{Nte}H$ complexes displayed the same differential binding affinities toward human mannosylated glycoproteins as those affinities previously determined by equilibrium binding analysis of FimCGH variants (Fig. 2C): A62S shows low affinity, WT displays intermediate or moderate affinity, and A27V/V163A exhibits high affinity for mannose. However, each of the binding-competent FimH variants displayed equal affinity for mannose when in a FimCH complex (*14*). Thus, we hypothesize that the observed adhesive differences among $FimG_{Nte}H$ complexes are the result of shifts in conformational equilibria of FimH in a tip-like setting caused by sequence variation. In summary, the $FimG_{Nte}H$ complex reliably functions as a minimal tip-like setting and appears well suited for the examination of FimH conformation by molecular biophysics.

Crystal structures of ligand-free $FimG_{Nte}H$ variants reveal diverse conformations in a tip-like setting

Apo x-ray crystal structures of $FimG_{Nte}H$ A62S and $FimG_{Nte}H$ A27V/V163A were solved at 1.96 and 2.6 Å resolutions, respectively, to investigate whether conformational changes determine the differences in mannose affinity of FimH in a tip-like setting. Both structures were solved by molecular replacement (MR) using $FimH_{PD}$ and either the low-affinity or high-affinity $FimH_{LD}$ from previously solved crystal structures as search models (table S1). The $FimG_{Nte}H$ A62S crystal structure reveals four $FimG_{Nte}H$ copies in the unit cell (fig. S1A), each adopting a **T** conformation (Fig. 2D). This **T** conformation is nearly equivalent to the **T** conformations of FimH (from *E. coli* strain F18) observed in (i) a FimCFFGH crystal structure (*17*) and (ii) the apo and heptyl mannoside–bound $FimG_{Nte}H$ crystal structures (fig. S2) (*26*). In these structures, $FimH_{LD}$ adopts the same overall compacted shape, widened β-sandwich fold, and displaced binding loops that confer weak affinity for mannose (fig. S2). However, structural alignment of $FimH_{PD}$ in the $FimG_{Nte}H$ A62S complex to $FimH_{PD}$ from the WT complexes in the **T** conformation exposes a ~7 Å rigid-body tilt of $FimH_{LD}$, suggesting a small vibrational degree of conformational flexibility in the **T** state. Despite this tilt, the **T** conformer of $FimG_{Nte}H$ A62S forms the same $FimH_{PD}$-$FimH_{LD}$ interface, in which hydrophobic interactions and interdomain hydrogen bonds bury the linker and an "insertion loop" (residues 109 to 124) (*17*) within a local hydrophobic core (Fig. 2E). Moreover, three of the four $FimG_{Nte}H$ A62S copies lack visible electron density in regions of mannose-binding loop 1 (residues 11 to 16), particularly at residues 13 and 14, suggesting that loop 1 is highly dynamic within the crystal (fig. S1B).

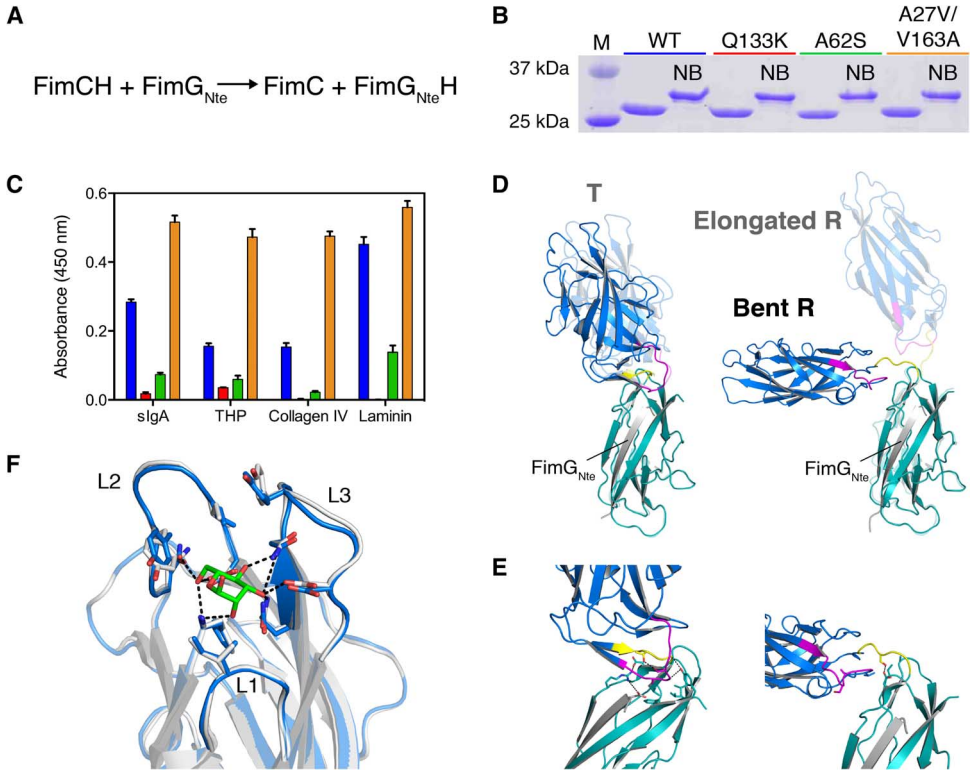

Fig. 2. Crystal structures and mannose binding of FimH variants in a tip-like setting. (**A**) Reaction scheme of in vitro DSE reaction to produce tip-like FimG$_{Nte}$H complexes. (**B**) Representative SDS–polyacrylamide gel electrophoresis of purified FimG$_{Nte}$H variants either boiled (not labeled) or not boiled (NB). (**C**) Enzyme-linked immunosorbent assay (ELISA) measuring binding of FimG$_{Nte}$H variant complexes to surface-coated glycoproteins, which include secretory IgA (sIgA), Tamm-Horsfall protein (THP), collagen IV, and laminin. (**D**) Crystal structures of FimG$_{Nte}$H A62S [Protein Data Bank (PDB) ID 5JQI, left] and FimG$_{Nte}$H A27V/V163A (PDB ID 5JR4, right) depicted as ribbons. These structures are overlaid on previously solved crystal structures of FimH in a FimCFFGH complex (3JWN) and FimCH complex (1KLF), respectively. Conformations are labeled accordingly. FimH$_{LD}$, linker, and FimH$_{PD}$ are colored as in (A), the insertion loop (residues 109 to 124) is colored purple, and FimG$_{Nte}$ is colored gray. (**E**) FimH$_{LD}$-FimH$_{PD}$ interface in FimG$_{Nte}$H A62S (left) and FimG$_{Nte}$H A27V/V163A (right). Contacts between residues are indicated as black dotted lines. (**F**) Structural alignment of FimG$_{Nte}$H A27V/V163A (colored blue) to FimH$_{LD}$ of mannose-bound FimCH (colored white). Residue side chains and mannose in green are depicted as sticks. Contacts between mannose and FimH are indicated as black dotted lines.

In contrast, the crystal structure of FimG$_{Nte}$H A27V/V163A reveals a novel **R** conformation, wherein the orientations of the FimH$_{LD}$ and FimH$_{PD}$ form a 90° bend (Fig. 2D). This observed conformation represents a substantial structural deviation from the elongated orientation of FimH$_{LD}$ and FimH$_{PD}$ observed in the **R** conformation of FimH bound to the FimC chaperone; thus, we refer to this crystal structure as the **bent R** conformation and the previously identified chaperoned state as the **elongated R** conformation (*15*). This **bent R** conformation is also distinct from a recently solved crystal structure of FimF$_{Nte}$H bound to heptyl mannoside, which shows FimH$_{LD}$ adopting a ~45° bend angle and a different orientation with respect to FimH$_{PD}$ (fig. S2) (*26*). Structural alignment of FimH$_{LD}$'s of the **bent** and **elongated R** conformations indicates that the FimH$_{LD}$'s of the two **R** structures are nearly identical [root mean square deviation (RMSD) = 0.6 Å], displaying the same binding loop and side-chain orientations that are required for high-affinity interactions with mannose (Fig. 2F) (*16*). Furthermore, the bent conformation exhibits a new interface between FimH$_{LD}$ and FimH$_{PD}$, composed of a dislodged insertion loop and an extended, solvent-exposed linker (Fig. 2E). No specific hydrogen bonding, electrostatics, or hydrophobic interactions are observed at this new interface, which would allow for a high degree of conformational flexibility in the relative orientations between FimH$_{LD}$ and FimH$_{PD}$ about the extended linker. Instead, multiple contacts formed between symmetry partners within the crystal lattice are coordinated by Ca^{2+}, which likely allowed for crystallographic trapping of the elusive **bent R** conformation (fig. S1, C and D). Comparison of the **bent R** conformation to the **T** conformation indicates that the orientation of FimH$_{LD}$ and FimH$_{PD}$ in the **bent R** conformation lies on a different bend and rotation axis than their orientation in the **T** conformation, hinting at considerable conformational freedom and possible transition pathways between **T** and **bent/elongated R** states. Together, these two FimH conformations (**T** and **bent R**) provide the first atomic-level description of a functionally diverse structural ensemble adopted by FimH in a native tip-like setting in the absence of ligand.

Positively selected residues and ligand binding modulate conformational ensembles of FimG$_{Nte}$H variants

Structural ensembles of FimH in solution were probed by small-angle x-ray scattering (SAXS) of FimH variants in FimG$_{Nte}$H or FimCH complexes. In a FimCH complex, all binding-competent FimH variants have the same affinity for mannose (*14*). They also appeared to adopt the same high-affinity **elongated R** conformation based on the structural comparison heat map (χ^2 = 0.4 to 0.6) (fig. S3, A and B) and rigid-body modeling of the FimCH crystal structure to the SAXS profiles for each of the FimCH variants (χ = 0.9 to 1.3) (fig. S3C). In contrast, each of these FimH variants had a drastically different affinity for mannose when in complex with FimG (Fig. 2C) (*14*). Correspondingly,

in the $FimG_{Nte}H$ complex, each variant adopted very different relative conformation(s) (χ^2 = 0.6 to 7.4), with the low-affinity A62S and high-affinity A27V/V163A variants being most dissimilar from one another (Fig. 3A). Further, radius of gyration (R_g) and maximal intramolecular distance (D_{max}) measurements indicated that A27V/V163A FimH is larger in overall shape by ~2 Å and more extended by ~5 Å than all other tested variants (Fig. 3B). Thus, we propose that positively selected residues allosterically influence the conformation(s) of FimH in pilus tips in solution, thus modulating mannose-binding affinity.

Binding of the $FimG_{Nte}H$ variants to a high-affinity mannose analog, termed mannoside 4Z269 (*27*), caused various degrees of conformational perturbation, with the WT variant undergoing the greatest change, as indicated by the structural comparison map (Fig. 3C). Upon binding 4Z269, all binding-competent $FimG_{Nte}H$ variants underwent a rightward shift in the pair distance distribution function [$p(r)$] with corresponding increases in D_{max} and R_g, suggesting extension of the shape of FimH (Fig. 3B). These changes were less pronounced for the A27V/V163A variant, which preexists in a high-affinity state. These effects were not observed in the control, binding null mutant Q133K. Ab initio models of the average conformation in solution, as represented by low-resolution molecular envelopes, revealed distinctive changes in overall protein shape among variants and between apo and 4Z269-bound states (Fig. 3D).

To resolve the solution structure(s) of FimH variants in a tip-like setting in the absence or presence of 4Z269, we evaluated the agreement between SAXS profiles and crystal structures of $FimG_{Nte}H$ in four distinct conformations [**T**, **bent R**, a previously identified distinct **bent R** (*26*), and **elongated R**] either individually or in combination with one another. Rigid-body modeling of individual structures (*28*) against these scattering profiles resulted in moderate-to-poor goodness of fit (χ = 2 to 10) (fig. S3D). In contrast, multistate rigid-body modeling determined specific weighted combinations of multiple conformational models that fit the data better than any individual model. This analysis indicated that in the absence of 4Z269, the A27V/V163A variant exists entirely in the **R** state, comprising a mix of **elongated** and **bent** shapes, whereas WT, Q133K, and A62S adopt various proportions of **T** and **bent R** states (fig. S3E). Addition of 4Z269 shifted the equilibrium away from the **T** conformation and toward a mix of **bent** and **elongated R** conformations for all variants except Q133K. However, multistate rigid-body modeling of SAXS profiles for $FimG_{Nte}H$ WT and A27V/V163A variants in the presence of 4Z269 resulted in moderate goodness of fit, which indicates that the four abovementioned static conformations do not completely represent the solution ensemble and implies additional solution conformations that have not been determined by crystallography. Together, the improvements in goodness of fit from multistate modeling strongly intimate a conformational equilibrium and suggest that the crystal structures used in rigid-body modeling likely represent conformational snapshots and may not necessarily represent "preferred" states or capture the expanse or diversity of the conformational space of FimH in solution. In agreement with the multistate modeling, differential scanning fluorimetry revealed a two-state unfolding behavior for apo $FimG_{Nte}H$ WT, Q133K, and A62S, with shifts toward one-state unfolding for A62S and WT variants in the presence of 4Z269 (fig. S3F). Single-state unfolding was observed for $FimG_{Nte}H$ A27V/V163A in the presence and absence of 4Z269. Together, these

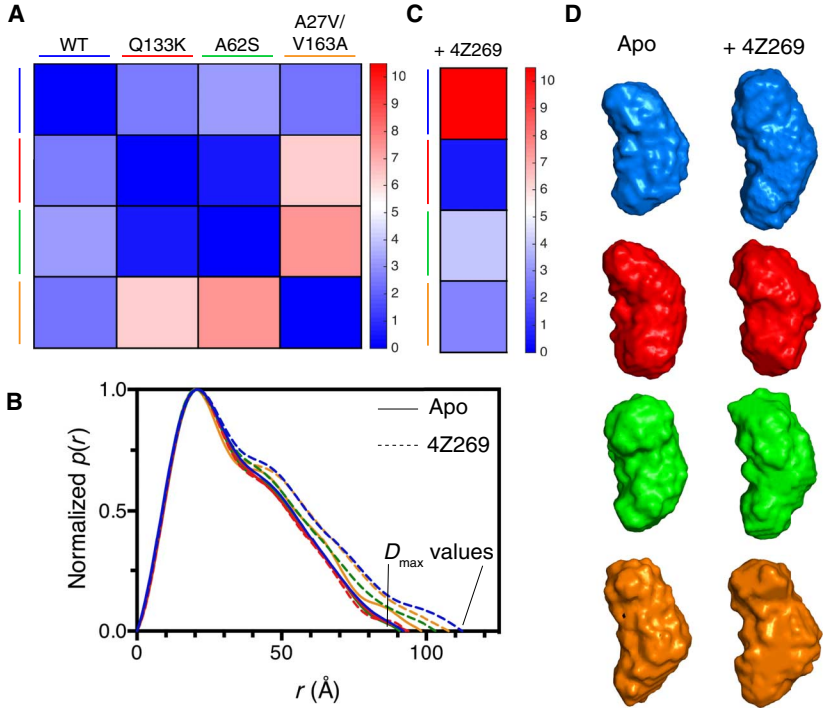

Fig. 3. Conformational ensembles of apo and ligated FimH variants in solution. (**A**) Structural comparison heat map of SAXS profiles indicates varying degrees of conformational similarity among $FimG_{Nte}H$ variants, as measured by χ^2, ranging from high (blue) to low (red) similarity. (**B**) Normalized pair distance distributions of $FimG_{Nte}H$ variants in the absence or presence of 4Z269. $FimG_{Nte}H$ variants are represented as solid lines in the absence of 4Z269 or dotted lines in the presence of 4Z269 and color-coded, as indicated by the colored lines in (A). (**C**) Structural comparison heat map indicates varying degrees of conformational similarity of each $FimG_{Nte}H$ variant in the absence or presence of mannoside 4Z269 at a 2× molar ratio. Color-coded as in (A). (**D**) Averaged ab initio models of $FimG_{Nte}H$ variants in the absence or presence of 4Z269 are color-coded, as previously indicated.

data strongly suggest that the identity of positively selected residues and mannose binding allosterically influence a preexisting equilibrium of distinct conformations in FimH in solution.

Further, ion mobility–mass spectrometry (IMMS) was used as a direct method to investigate conformational distributions of FimH due to the ability of IMMS to resolve protein collision cross sections (CCSs). All $FimG_{Nte}H$ and 4Z269-bound $FimG_{Nte}H$ complexes remained intact when they were electrosprayed into the mass spectrometer, facilitating downstream analysis of the tip-like setting by IMMS (fig. S4, A and B). The CCS distributions at low collision energy (CE) of the WT, Q133K, and A62S variant $FimG_{Nte}H$ complexes revealed a major peak and shoulder, whereas only one predominant peak with positive skew was observed for the A27V/V163A variant (Fig. 4A). Comparison of these distributions indicated that the A27V/V163A distribution is shifted to the right (or "right-shifted") and displays a greater mean CCS than do the other variant distributions, consistent with its larger average shape (by R_g and D_{max}) in solution. Given their non-normal shape, these distributions were modeled as a sum of two Gaussian curves. The WT, Q133K, and A62S $FimG_{Nte}H$ complexes were each similarly best explained by two curves that have mean CCS values of 2464 to 2472 $Å^2$ and 2606 to 2636 $Å^2$, which we respectively label ***A*** and ***B*** (Fig. 4B and table S2). In contrast, the A27V/V163A $FimG_{Nte}H$ profile was best explained by two highly overlapping curves with mean CCS values of 2480 and 2565 $Å^2$, which we respectively label ***A*** and ***C*** given their positions relative to the curves assigned for the other three FimH variants. Binding of 4Z269 caused a rightward shift in the overall CCS distributions of WT, A62S, and A27V/V163A (Fig. 4B). 4Z269-bound WT and A62S $FimG_{Nte}H$ displayed CCS distributions with right-shifted ***A*** and right-shifted ***B***, indicating that the two major structural species can engage 4Z269. In contrast, 4Z269-bound A27V/V163A $FimG_{Nte}H$ displayed a normal CCS distribution adequately explained by one well-fitting curve because modeling with two Gaussian curves indicated that right-shifted ***A*** and ***C*** overlap too extensively for an unambiguous assignment. As expected, no $FimG_{Nte}H$ Q133K:4Z269 complex was observed (fig. S4B). In all cases, CCS distributions steeply increased with elevation of CE, indicative of protein unfolding and confirming that the CCS distributions analyzed above represent folded protein conformations (fig. S4C). In summary, $FimG_{Nte}H$ WT, Q133K, and A62S in the gas phase take on an equilibrium of two distinct conformations with partially overlapping CCS distributions, whereas $FimG_{Nte}H$ A27V/V163A adopts an equilibrium of two very similar conformations with highly overlapping CCS distributions. Thus, we have resolved two to three different structural conformations among $FimG_{Nte}H$ variants in the gas phase. However, the width of the measured CCS distributions and mixture of structural populations likely mask multiple underlying conformational substates that dynamically interconvert within this conformational landscape. The conformational states represented by peaks ***A***, ***B***, and ***C*** may relatively correspond to **bent R**, **T**, and **elongated R** states, respectively, but a detailed examination of the presumed conformational dynamics of the **T** and **R** states is necessary to assess the validity of these structural assignments.

$FimG_{Nte}H$ samples expansive conformational phase space composed of restrained T state and dynamic R state

To gauge the dynamic behavior of FimH in the $FimG_{Nte}H$ WT tip-like setting, we performed unrestrained molecular dynamics (MD) simulations in four replicates, each starting from the **T**, **bent R**, and **elongated R** conformations in the presence or absence of ligands. MD trajectories initiated from the **T** state revealed very little structural fluctuation (RMSD) over time, vibrating around a fixed protein shape (R_g distribution), whereas those initiated from the **bent R** state carved a vast conformational landscape with various overall protein shapes (Fig. 5A and movies S1 and S2). To best compare and conceptualize the sampled conformational landscapes, we parameterized $FimG_{Nte}H$ conformation within a phase space composed of three measurable angular dimensions: (i) bend, (ii) twist, and (iii) orientation

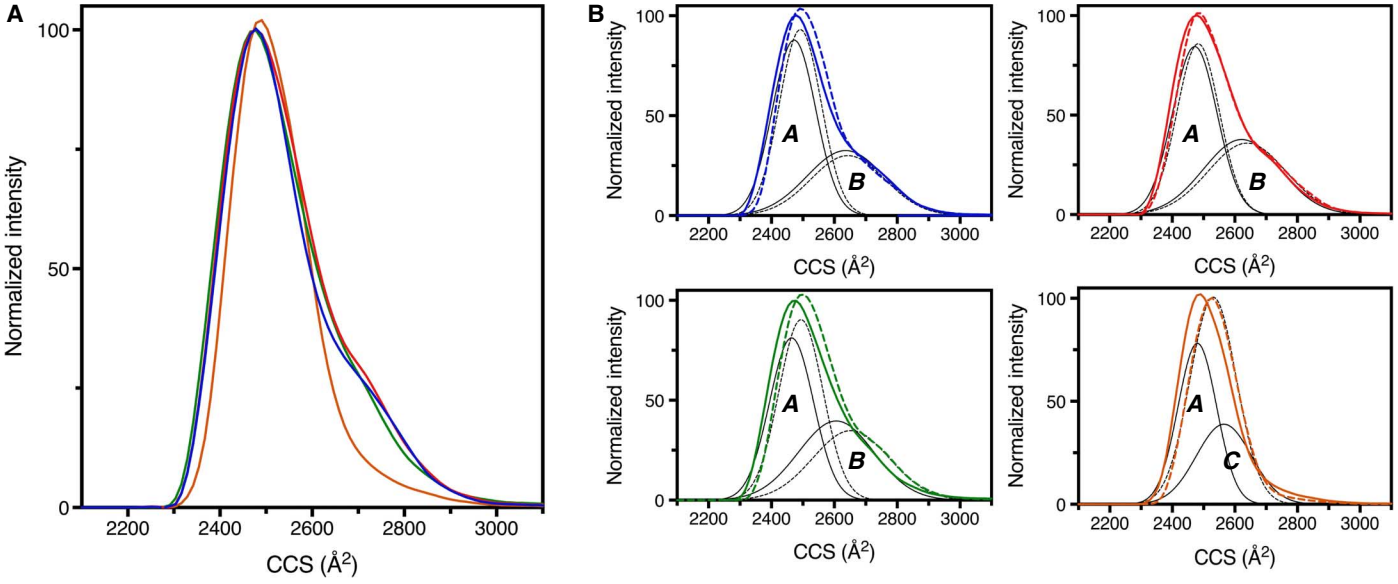

Fig. 4. Conformational distributions of free and 4Z269-bound $FimG_{Nte}H$ variants isolated in the gas phase, as revealed by IMMS. (**A**) CCS distributions of intact $FimG_{Nte}H$ variant complexes measured by IMMS. (**B**) Comparison of CCS distributions of free (solid line) and 4Z269-bound (dotted line) $FimG_{Nte}H$ variants. The solid and dotted black lines represent fitted Gaussian distributions to apo and ligated $FimG_{Nte}H$, respectively. Fitted Gaussian distributions are labeled by letters, given their mean CCS values. Note that Q133K cannot bind mannose and that the dotted lines for this variant represent CCS distributions and Gaussian fits to an independently measured apo $FimG_{Nte}H$ Q133K spectral peak from the sample that was treated with 4Z269.

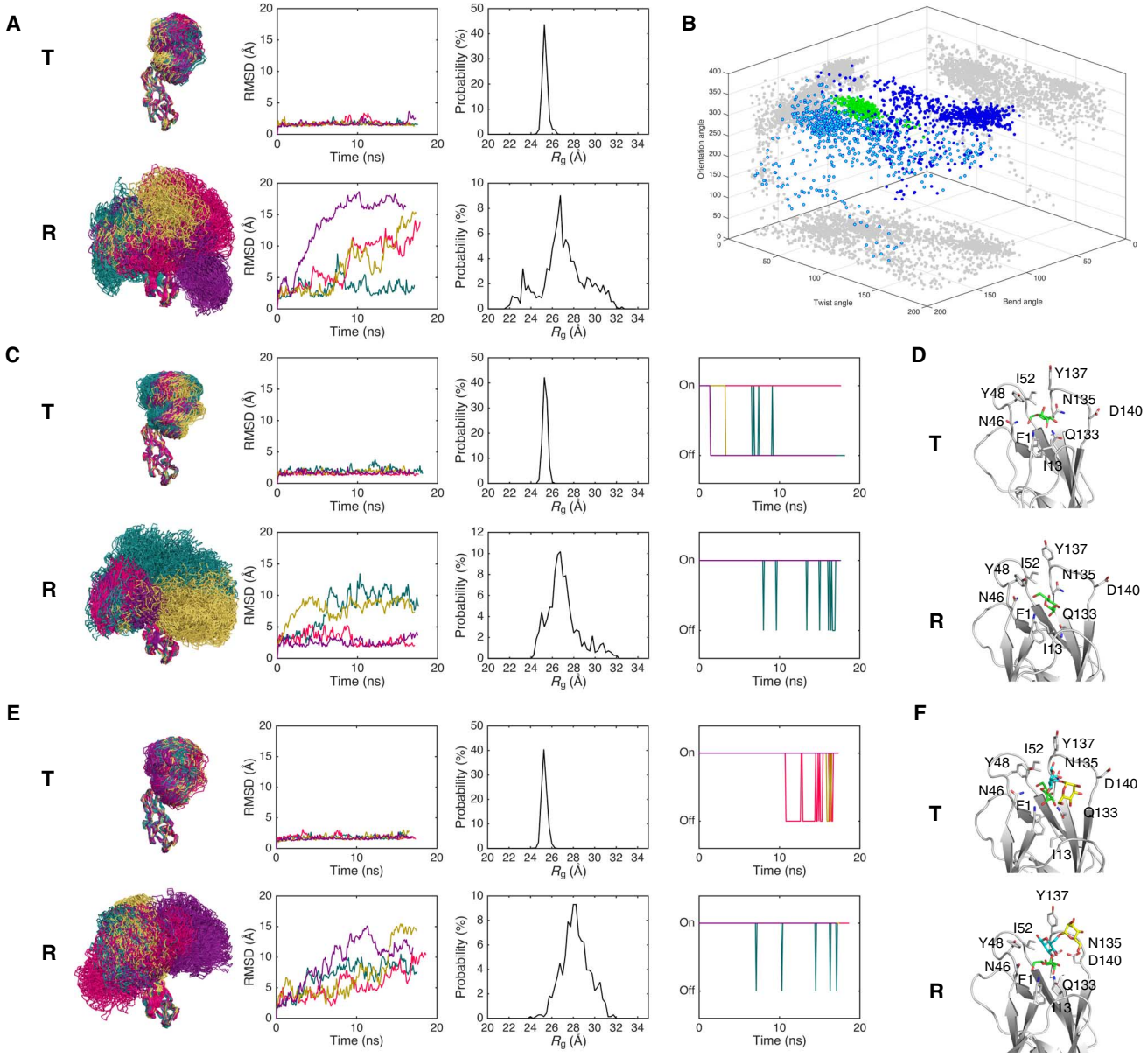

Fig. 5. Dynamics and binding mechanisms of conformational populations in $FimG_{Nte}H$ WT. (**A**) Structures revealed by MD simulations of $FimG_{Nte}H$ WT in a **T** conformation (top) or **bent R** conformation (bottom) with corresponding measures of structural fluctuation over time (RMSD) and distributions of sampled protein shapes (R_g). Different colors correspond to four independent simulation replicates. (**B**) Three-dimensional conformational phase space of $FimG_{Nte}H$ as defined by bend, twist, and orientation angles for simulations initiated from the **T** (green), **bent R** (blue), or **elongated R** (cyan) conformation. Shadows are cast on the grid panels and colored in gray. (**C**) Structures revealed by MD simulations of $FimG_{Nte}H$ WT in a **T** conformation (top) or **bent R** conformation (bottom) in the presence of mannose, with corresponding measures of structural fluctuation over time (RMSD), distributions of sampled protein shapes (R_g), and mannose binding. "On" and "Off" measure whether the center of mass of mannose is within or outside 10 Å of the carbonyl of residue F1 in the binding pocket. (**D**) Representative binding modes of mannose for **T** (top) and **bent R** (bottom) after 5 ns. Mannose is depicted as sticks, whereas FimH is shown as a ribbon representation. (**E**) Structures revealed by MD simulations of $FimG_{Nte}H$ WT in a **T** (top) or **bent R** (bottom) conformation in the presence of oligomannose-3 (Man(α1–3)-[Man(α1–6)]-Man), with corresponding measures of structural fluctuation over time (RMSD), distributions of sampled protein shapes (R_g), and mannose binding. "On" and "Off" measure whether the center of mass of oligomannose-3 is within or outside 20 Å of the carbonyl of residue F1 in the binding pocket. (**F**) Representative binding modes of oligomannose-3 for **T** (top) and **bent R** (bottom) after 8.5 ns. Man(α1–3)-[Man(α1–6)]-Man is depicted as sticks and colored green, yellow, and cyan, respectively.

of $FimH_{LD}$ relative to $FimH_{PD}$ (fig. S5A). This analysis showed the breadth of conformations sampled in the **R** state compared to the restrained phase space of the **T** state simulations (Fig. 5B). Motions among the **R** conformations resembled movement about a ball-and-socket joint, in which a wide range of bends and rotations are accessible but restrained by the architecture of the $FimH_{LD}$ and $FimH_{PD}$ interface, which functions as a "socket." We also observed considerable overlap in phase spaces from simulations initiated from the **bent** and **elongated R** states (Fig. 5B and movies S2 and S3), but no exchange between **T** and **R** states under these in silico conditions or in preliminary

trials at 200 to 600 ns, suggesting a high-energy barrier to transition between **T** and **R** states that occurs on a much longer time scale (microseconds to milliseconds). Thus, the **bent** and **elongated R** conformations represent distinct snapshots of a highly dynamic conformational state, whereas the **T** conformation is a snapshot of a conformationally restrained structural state, which argues for enthalpy-entropy compensation in the equilibrium between **T** and **R** states.

Mannose was then included in simulations of $FimG_{Nte}H$ WT to probe its effect on conformational dynamics and mechanisms of ligand binding. The presence of mannose did not significantly alter the simulated dynamic behaviors of the **T** and **R** states (Fig. 5C and movies S4 to S6). Strikingly, the **R** states remained bound to mannose even during the bending, twisting, and rotation that occured between the two domains throughout the duration of the simulations (Fig. 5C and movies S5 and S6). As expected, the **R** states oriented their binding pocket loops to clasp mannose tightly with rare, short-lived dissociation events, a signature of high-affinity binding (Fig. 5, C and D). Mannose sat in the **R** pocket rigidly in a "horizontal" orientation, held in place by hydrogen bonds to residues in loop 2 (N46 and D54) and loop 3 (Q133, N135, and D140) and through packing against I13, I52, and the "tyrosine gate" (defined as binding pocket residues Y48 and Y137), as previously observed (*16*). In contrast, **T** states weakly interacted with mannose, characterized by continual motion of mannose within the open **T** pocket and multiple, long-lasting dissociation events (Fig. 5C and movie S4). When bound to the **T** state, the mannose ring occasionally sampled the horizontal orientation, as observed in the pocket of the bound **R** state, but was primarily observed rotated ~45° relative to its horizontal orientation (Fig. 5D). In the **T** state pocket, the hydroxyl group off the achiral carbon (C6) of mannose was bound to the N terminus of FimH and the carboxyl side chain of FimH residue D54. These two interactions were also observed with mannose bound to FimH in the **R** state. In contrast to what was observed in the **R** state, the axial hydroxyl group off the mannose anomeric carbon (C1) faced away from the rest of the binding pocket. This "tilted" mannose orientation represents a unique bound conformation and provides the first mechanistic insights into how the **T** state may contribute to host-pathogen interactions. FimH engages complex mannose-containing glycans on glycoproteins expressed on host epithelial cells (*29*, *30*). Thus, to have biological significance, the tilted mannose orientation must allow stereochemical space for FimH to engage the mannose-containing glycan without steric clashes with the extended glycan chain. Simulations indicated that oligomannose-3 (Man(α1–3)-[Man(α1–6)]-Man) approached and bound the **T** state pocket in either the tilted or horizontal orientation with about equal frequency, revealing the sterically unhindered manner in which the **T** state can engage oligomannose receptors (Fig. 5, E and F, and movie S7). As expected, oligomannose-3 bound to the **R** state only sampled the horizontal orientation (Fig. 5, E and F, and movie S8). Docking of oligomannose-3-chitobiose (Man(α1–3)-[Man(α1–6)]-Man(β1–4)-GlcNAc(β1–4)-GlcNAc) to distinct time points within the **T** state simulations indicated that the 1–3 branched terminal mannose of the oligomannose epitope is capable of freely rotating by ~45° within the binding pocket to allow for intercalation of the Man-GlcNAc moiety within the sterically accessible, dynamic tyrosine gate (fig. S5B). Previous crystallographic studies and isothermal titration calorimetry experiments indicate that the tyrosine gate displays a high degree of conformational dynamics in the presence of hydrophobic functional groups, such as those within the aglycon moiety of mannosides (*31*). Thus, the proposed ligand entry and rotation pathways may represent a stepwise mechanism through which induced-fit binding proceeds, whereby interactions in the **T** state trigger structural perturbations within $FimH_{LD}$ that culminate in **T**-**R** conformational changes.

Comparison of the distributions of binding loop and residue positions among apo **T**, mannose-bound **T**, apo **R**, and mannose-bound **R** states for WT $FimG_{Nte}H$ revealed specific motions that are correlated with mannose binding (fig. S5C). Among these changes, movement of loop 1 toward the binding pocket was most strikingly associated with mannose binding in the **R** state but marginally so in the **T** state. Despite the occasional displacement of loop 1 away from the **R** pocket, mannose often remained stably associated with **R**, suggesting that loop 1 positioning is not the only determinant of mannose binding. Consistent with this observation, binding assays performed on loop 1 deletion mutants and chimeras in WT $FimH_{LD}$ showed a significant reduction, but not total abrogation, in mannose binding, demonstrating a role for loop 1 as an affinity clamp in mannose recognition (fig. S5D). These findings agree with the weakened mannose affinity observed in mutations upstream of loop 1 that prevent β-hairpin formation necessary to bring loop 1 in close proximity to the binding pocket and observed in a recent cocrystal structure showing loop 1 in close proximity to heptyl mannoside in a bound **T** state due to stabilization from crystal packing (*26*, *32*). In all, these computational studies establish a vast conformational phase space in the absence of ligand characterized by a conformationally restrained **T** state and multiple, shape-shifting **R** state conformations, and they elucidate structural and dynamic insights into two distinct mechanisms of mannose recognition by the low-affinity **T** and high-affinity **R** conformations.

Positive selection in FimH promotes moderate mannose-binding affinity to facilitate bladder colonization

Positively selected residues, which were identified through sequence analysis of FimH alleles enriched in urinary *E. coli* isolates, significantly affect adhesive function and bacterial fitness in the urinary tract (*13*). Despite A27V/V163A existing entirely in the high-affinity **R** state, previous work paradoxically demonstrated that UTI89 engineered to encode FimH A27V/V163A in place of FimH WT was severely attenuated and unable to form IBCs in the C3H/HeN mouse model of UTI at 6 to 24 hours post-infection (hpi) (*13*, *14*). We investigated the kinetics of this virulence defect during the acute stages of bladder colonization. UTI89 expressing A27V/V163A FimH exhibited attenuated colonization as early as 1 hpi, which suggests a defect in the ability of A27V/V163A to bind and/or invade superficial facet cells (Fig. 6A). Yet, UTI89 expressing A27V/V163A FimH bound and invaded 5637 bladder cells in vitro more efficiently than UTI89 expressing WT FimH (Fig. 6, B and C), suggesting that the high-affinity variant does not lack the capacity to bind bladder tissue per se. 5637 bladder cells, a cancer cell line, exhibit more similarities with undifferentiated transitional bladder epithelial cells than with the terminally differentiated superficial facet cells that line the undisrupted bladder lumen (*33*). Thus, attenuation in the mouse model may reflect colonization resistance properties of the bladder habitat that are specifically selective against A27V/V163A FimH over WT FimH. To address this hypothesis, we changed the bladder habitat by inserting a catheter implant and subsequently tested these FimH variants in a model of catheter-associated UTI (CAUTI). In this model, a 5-mm piece of silicon tubing is implanted into the C57BL/6 mouse bladder, which mechanically disrupts regions of the bladder epithelium, exposing the underlying transitional epithelium and inducing inflammation. It has previously been shown that this catheterization increases the efficiency of bladder colonization by otherwise attenuated species of bacteria (*34*–*37*). In the absence of an implant, again, a colonization

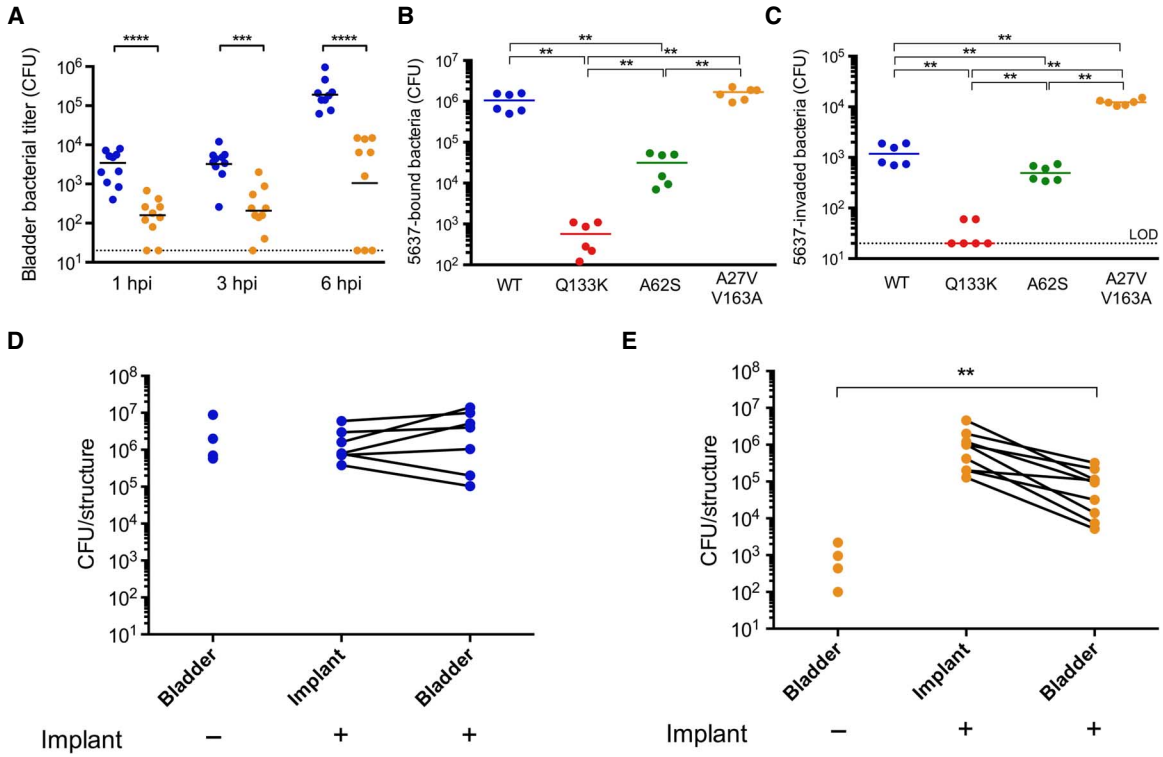

Fig. 6. Role of FimH conformation in bladder colonization during UTI. (**A**) Bacterial titers of mouse bladders infected with UTI89 harboring either FimH WT (blue) or A27V/V163A (orange) at an inoculum of 10^7 colony-forming units (CFU) measured at 1, 3, and 6 hpi. (**B**) Total bacterial titers of 5637 bladder epithelial cells (no gentamicin treatment) infected with UTI89 harboring WT (blue), Q133K (red), A62S (green), or A27V/V163A (orange) FimH at an inoculum of 10^7 CFU. (**C**) Invaded bacterial titers of 5637 bladder epithelial cells (treated with gentamicin) infected with UTI89 harboring WT (blue), Q133K (red), A62S (green), or A27V/V163A (orange) FimH at an inoculum of 10^7 CFU. LOD, limit of detection. (**D** and **E**) Bacterial titers of C57BL/6 mouse bladders without catheterization or bladders and implants infected with UTI89 harboring either FimH WT (blue) or A27V/V163A (orange) at an inoculum of 10^7 CFU 24 hours after catheterization. $^{**}P < 0.01$, $^{***}P < 0.001$, $^{****}P < 0.0001$, two-tailed Mann-Whitney *U* test.

defect was observed in C57BL/6 mice at 24 hpi (Fig. 6, D and E). Within this CAUTI model, in the presence of an implant, UTI89 with either WT or A27V/V163A FimH robustly colonized both the implant and the implanted mouse bladder tissue at 1 day after infection, although this rescue was partial because WT still outperformed A27V/V163A by 10-fold in bacterial titers in the bladder (Fig. 6, D and E). How the implant facilitates colonization may be multifactorial. First, disruption of the terminally differentiated epithelium may allow bacteria expressing the A27V/V163A variant to bypass the intact superficial facet cell layer and colonize deeper epithelial layers. Second, the catheter provides another surface to which the bacteria can bind and form a "staging ground" for dissemination to the bladder tissue. This is particularly possible because implanted catheters become coated by host proteins, including THP (*36*, *38*), which we have shown is tightly bound by A27V/V163A (Fig. 2C). In addition, A27V/V163A can directly interact with implanted catheters, and in vitro assays indicate that it forms biofilms on abiotic surfaces to a higher degree than does WT (*13*). In contrast, without the catheter, the tighter binding to soluble THP, or other soluble host proteins or mannose-containing oligosaccharides, by A27V/V163A may be particularly detrimental to colonization because it prevents binding to urinary tract surfaces. Thus, in the naive bladder, soluble host proteins and oligosaccharides may act as decoy receptors, whereas in the catheterized bladder, soluble host proteins may aid in binding of bacteria to the implant. Together, these studies demonstrate that the preexisting conformational ensemble and corresponding mannose affinity of FimH determine the outcome of infection. Further, the results suggest that positive selection balances the conformational equilibrium of FimH in solution between **R** and **T** states to tailor moderate affinity to UPEC for the urothelium, thus facilitating adherence to and persistence in the bladder.

DISCUSSION

Our interdisciplinary studies combining evolutionary biology and computational and molecular biophysics allowed us to directly interrogate, at the atomic and structural level, the multiple conformations that FimH adopts in solution in a tip-like setting within a two-state, **T**-**R** conformational landscape (Fig. 7A). Positively selected residues influence the preexisting conformational equilibrium of the two-domain FimH by shifting the relative occupancies of a dynamically restrained **T** state conformation and multiple **R** state conformations that sample a great expanse of bends, twists, and orientations through ball-and-socket joint-like motions. As a result of these population shifts, natural sequence variation alters the apparent affinity of FimH toward mannosylated ligands. Thus, the conformational phase space of FimH in solution and population shifts spurred by positively selected residues further provide a framework for understanding the structural basis of allosteric coupling between interdomain interactions and mannose binding. Classically, the mechanism underlying protein allostery has been conceptualized as a deterministic process, in which information is transmitted through structural perturbations from one site of a protein to another in a sequential or concerted manner (*39*–*41*). However,

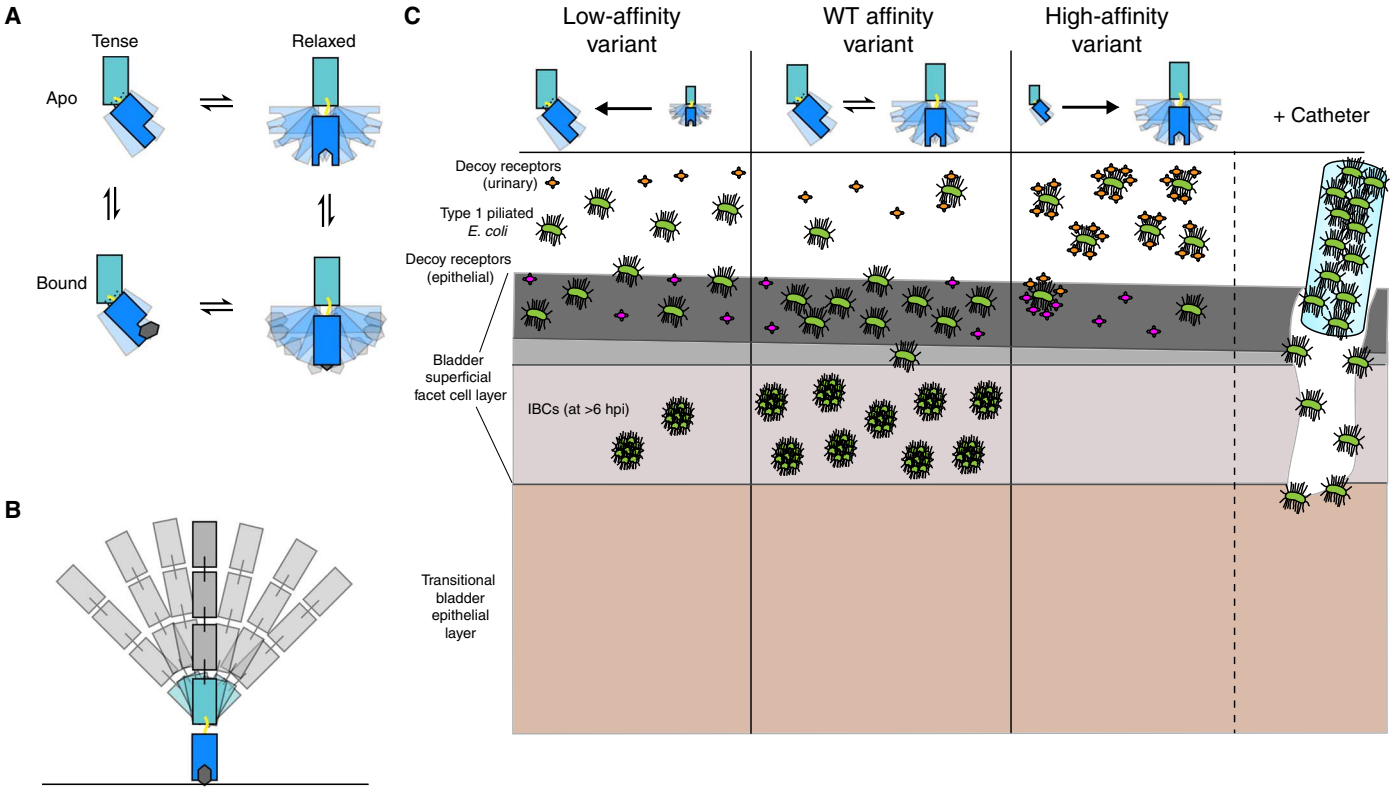

Fig. 7. Proposed model of FimH conformational ensembles, mannose binding, and virulence in UTI. (**A**) Two-state conformational landscape of FimH. FimH at the pilus tip natively adopts an equilibrium of a single, dynamically restrained, low-affinity **T** state and multiple, highly dynamic, high-affinity **R** states with various bends, twists, and orientations. Positively selected residues can shift this preexisting conformational equilibrium and thereby influence mannose-binding affinity. The **T** and **R** states can bind mannose. Mannose in a tilted orientation rapidly enters into the widened and shallow binding pocket of the **T** state. Mannosylated ligands in a bound **T** state can then rotate in a high-affinity orientation and allosterically trigger structural perturbations that disrupt $FimH_{LD}$ and $FimH_{PD}$ interactions and facilitate conversion to the bound **R** state. In addition, mannose in a horizontal orientation can less rapidly engage the **R** state but does so very tightly through hydrogen bond interactions with several binding loop residues. Positive selection, in modulating a native conformational equilibrium, likely alters flux through these two distinct binding mechanisms. (**B**) Schematic model of the FimH molecular tether. The bends, twists, and orientations between $FimH_{LD}$ and $FimH_{PD}$ adopted in bound **R** states argue for a model in which the pilus tip can bend and rotate at the site of the FimH linker with an immobilized, bound $FimH_{LD}$. This physical tethering in theory increases the biophysical and functional adaptability of the pilus and thereby allows bacteria to remain attached to the bladder epithelium. (**C**) Pathogenesis outcomes depend on the preexisting equilibrium and affinity of FimH, whereby moderate affinity is ideal for successful colonization of the bladder epithelium and formation of IBCs. Catheterization allows the high-affinity variant A27V/V163A to partially circumvent the colonization resistance property observed in the intact, unperturbed bladder habitat.

recent synergy in the fields of protein biophysics and protein evolution has given rise to the emerging perspective that protein allostery is a natural and statistical consequence of shifts in the relative populations and/or dynamics of preexisting conformational ensembles (*42*, *43*), which is supported by this work. Furthermore, by influencing the preexisting equilibrium of FimH, positively selected residues alter the very pathway through which binding occurs: If a particular FimH variant favors the **T** state, it will favor an induced-fit mechanism of binding; if a FimH variant favors the **R** state, it will use conformational selection as its mechanism of binding.

Our structural, biophysical, and computational work indicate that the low-affinity **T** and high-affinity **R** conformations can bind mannose through distinct binding orientations and pathways. Consistent with previous cocrystal structures, simulations of the **R** state indicate that mannose and oligomannose-3 bind in a high-affinity horizontal orientation coordinated through hydrogen bond formation with residue F1 and residues in loops 2 and 3 and clamped by residue I13 in loop 1. Our simulations and a recent crystal structure of the **T** state bound to heptyl mannoside (*26*) also indicate that the **T** state may bind mannose in this horizontal orientation, particularly when loop 1 is proximal to the binding pocket. In addition to this binding mode, mannose also approaches and binds the **T** state pocket in a tilted orientation, specifically to residue F1 of the N terminus and D54 of loop 2, in a low-affinity interaction. Mannose glycans may slide and rotate and interact with the conformationally dynamic tyrosine gate of FimH. This novel ligand entry and rotation pathway may represent a stepwise mechanism through which induced-fit binding proceeds, whereby interactions in the **T** state trigger structural perturbations within $FimH_{LD}$ that culminate in **T**-**R** conformational changes. Furthermore, tight binding of mannose through multiple different bends and orientations of the **R** state, as indicated in our simulations, provides the basis for a physical model, here termed molecular tethering, by which bacteria can remain bound to their mannosylated receptors on the bladder surface (Fig. 7B). Entropic freedom of multiple bound conformations within the high-affinity **R** state would theoretically enhance the lifetime of mannose binding relative to a single high-affinity **R** state. Moreover, the enhanced conformational flexibility and the number of viable bound **R** conformations in FimH may increase the biophysical adaptability of

type 1 pili while tethered to a surface in part to allow attached bacteria to resist urine flow while bound to the bladder epithelium (*44*, *45*). Molecular tethering likely represents a universal feature of macromolecular interactions involving Gram-negative adhesins or any other two-domain, allosterically regulated protein containing a flexible linker.

Coupled with genetic and in vivo pathogenesis work, we have demonstrated how evolutionary pressures through positive selection in FimH allosterically shape the conformational dynamics and phase space of FimH to maintain a balanced conformational equilibrium between **R** and **T** states to allow UPEC to colonize the urinary tract (Fig. 7C). Surprisingly, a FimH variant that only adopts the high-affinity **R** state is severely attenuated early in a mouse model of uncomplicated UTI but is proficient at colonizing catheterized bladders in vivo or bladder transitional-like epithelial cells in vitro. Given how early the pathogenesis defect of A27V/V163A is observed relative to WT (within 1 hpi), some preset aspect(s) of the bladder habitat likely select against the high-affinity **R** conformation(s). One possibility may relate to the slower kinetics of association of the **R** state under conditions of flow, as part of a catch-bond mechanism (*44*–*46*), which, in the case of A27V/V163A, would translate to less frequent interactions with the bladder epithelium and increased clearance of bacteria from the bladder during periods of urination. A second possibility is that some inherent property of the bladder epithelium serves as a restrictive factor against the **R** state. We suggest that the superficial facet cells may mediate this restriction, because the A27V/V163A variant is capable of binding 5637 bladder cells in vitro and can mediate the colonization of the catheter-implanted bladder habitat. A third possibility is that soluble mannosylated glycoproteins, such as THP, and mannose-containing oligosaccharides (*47*) may serve as decoy receptors that reduce the ability of A27V/V163A to colonize the bladder epithelium because it binds more tightly than WT to THP. These same host proteins that serve as decoys in host defense may facilitate bacterial colonization by coating the catheter (*36*, *38*). More work is required to dissect the individual and combinatorial contributions that the abovementioned possibilities may exert in preventing the high-affinity **R** state in mediating successful bladder colonization. Together, our data suggest that the **T** state may serve to temporarily mask the strong affinity that FimH has for mannose to avoid restrictive factors or properties native to the bladder habitat to initiate productive binding when engaging the host epithelium.

Fundamentally, this encompassing study of solution protein dynamics, structure, and function exemplifies the importance of defining the native conformational ensembles of a protein in solution and its population shifts in the presence of ligand for a complete model of allosteric regulation. Understanding mechanistic and structural aspects of adhesin allostery, conformation, and function is critical in efforts to further develop antibiotic-sparing small molecules and vaccines for the treatment of acute and recurrent infections caused by UPEC and other pathogens.

MATERIALS AND METHODS

Ethics statement

All animal experiments were conducted according to the National Institutes of Health (NIH) *Guide for the Care and Use of Laboratory Animals* and performed in accordance with institutional regulations after pertinent review and approval by the Animal Studies Committee at Washington University School of Medicine (protocol number 20150226). Human urine collection was performed with informed consent and approved under Institutional Review Board protocol 201207143.

FimH variants

In silico analysis of FimH sequences among 287 *E. coli* strains previously revealed three specific residues (positions 27, 62, and 163) evolving under positive selection. Variations at these three positions in the FimH sequence from UPEC strain UTI89 were examined in this study. These include the following: (i) the WT variant (A27/A62/V163), in which these three amino acids are together observed in *E. coli* isolates from infected urine (19 of 254 strains) but not in isolates from healthy feces (0 of 33 strains); (ii) the A62S variant (A27/S62/V163), in which these three amino acids are together observed in high abundance in isolates from both infected urine (169 of 254 strains) and healthy feces (28 of 33 strains); and (iii) the engineered A27V/V163A variant (V27/A62/A163), in which these three amino acids have not been observed in tandem and have been shown to negatively affect pathogenesis in vivo. The mannose-binding pocket mutant Q133K, which cannot bind mannose, was also incorporated in this study as a negative control. These variants were generated by site-directed mutagenesis of the WT FimH allele from UTI89, as described in a previous report (*13*).

Protein expression and purification

FimCH variant complexes were purified from periplasm preparations, as previously described (*14*). $FimG_{Nte}H$ complexes were assembled by a spontaneous in vitro DSE reaction, in which $FimG_{Nte}$ peptide (FimG residues 1 to 15; EZBiolab) was mixed in ~10× molar excess with FimCH variant complexes in 15 mM MES (pH 5.6) and 50 mM NaCl and incubated at 37°C for 16 hours. $FimG_{Nte}$ displaces FimC in this reaction, and resultant $FimG_{Nte}H$ variant complexes were purified away from excess $FimG_{Nte}$ peptide and free FimC using a SOURCE 15S column (GE) in 15 mM MES (pH 5.6) with a gradient of 0 to 400 mM NaCl. Pooled fractions containing $FimG_{Nte}H$ variant complexes were dialyzed against 15 mM MES (pH 5.6) and 50 mM NaCl, concentrated to 1 to 5 mg/ml, and stored stably at 4°C for use in biophysical assays.

Mannoside incubations

Mannoside compound 4Z269 (*para*-biphenyl-2-methyl-3′-methyl amide mannoside) (*27*) was incubated with $FimG_{Nte}H$ variant complexes for at least 1 hour at 4°C before biophysical analysis at molar ratios indicated below.

Differential scanning fluorimetry

$FimG_{Nte}H$ variants (10 μM) in the absence or presence of 4Z269 (10 μM) were combined with 5× SYPRO Orange (Sigma; 1:1000 dilution of 5000× stock) in 50 μl of reaction mixture buffered in 15 mM MES (pH 5.6), 50 mM NaCl, and 0.4% dimethyl sulfoxide. Binding equilibria were established by allowing the reaction mixtures to incubate at 23°C for 30 min. These reaction mixtures were then placed in 96-well clear-bottom polymerase chain reaction plates and subjected to a melt curve from 20° to 90°C in 0.5°C increments of 15 s, each followed by a fluorescence read of the "HEX" channel in a Bio-Rad CFX96 thermocycler. Melt curves were fitted to the Boltzmann equation [$y = A_2 + (A_1 - A_2)/(1 + \exp((x - x_o)/dx))$, where x_o is the T_m] to determine the melting temperature (T_m).

Enzyme-linked immunosorbent assay

Immulon 4HBX 96-well plates were coated overnight with 1 μg of human glycoproteins reported to be ligands of FimH (secretory IgA, laminin, collagen IV, and THP). All glycoproteins were ordered from

Sigma except crude THP, which was isolated by ammonium sulfate precipitation of urine donated by healthy volunteers. Coated wells were then incubated with 200 µl of blocking buffer [phosphate-buffered saline (PBS) + 2% bovine serum albumin (BSA)] for 2 hours at 23°C, followed by incubation with 100 µl of $FimG_{Nte}H$ variants diluted in blocking buffer to 1 µg/ml for 1 hour at 37°C. After washing three times with PBS + 0.05% Tween 20, 100 µl of polyclonal rabbit antibody raised against FimH residues 1 to 165 (from *E. coli* strain J96) with a C-terminal six-histidine tag (Sigma Genesis; 1:5000 dilution in PBS + 2% BSA) was added to each well for 1 hour at 37°C. After washing three times with PBS + 0.05% Tween 20, 100 µl of polyclonal goat anti-rabbit antibody conjugated to horseradish peroxidase (KPL; 1:5000 dilution in PBS + 2% BSA) was added to each well for 1 hour at 37°C. After a final round of washing, plates were developed with 100 µl of tetramethylbenzidine substrate (BD Biosciences) and quenched within 1 min with 50 µl of 1 M H_2SO_4, and absorbance was measured at 450 nm.

Small-angle x-ray scattering

Before sample submission, FimCH and $FimG_{Nte}H$ variant complexes were buffer-exchanged three to five times in Spin-X UF 5K concentrators (Corning) against freshly prepared buffer [15 mM MES (pH 5.6) and 50 mM NaCl] to a final concentration of 5 to 8 mg/ml. $FimG_{Nte}H$:4Z269 complexes were prepared in the same manner after $FimG_{Nte}H$ variants were incubated with 4Z269 at a 1:2 molar ratio. Samples were diluted to 1 to 5 mg/ml using the final filtrate to ensure identical buffer conditions between buffer and sample. Samples were then shipped to the SIBYLS beamline at the Advanced Light Source for data collection and basic data processing, including scattering integration and buffer subtraction, as detailed extensively in the high-throughput mail-in SAXS protocol (*48*). Integrated scattering profiles were then inspected and analyzed using the ATSAS program suite (*49*). At least 9 to 12 scattering profiles representing multiple concentrations and exposures were merged in PRIMUS to generate an average scattering profile for each sample tested. Pair distance distributions [$p(r)$] and maximal intramolecular distances (D_{max}) were determined by GNOM. Structural comparison maps were calculated, as previously described, using the SIBYLS SAXS Similarity online tool (http://sibyls.als.lbl.gov/saxs_similarity/) (*50*). Fits of crystal structures to merged scattering profiles were evaluated by the FoXS and MultiFoXS servers in the case of single-state and multistate rigid-body modeling, respectively. For each sample, 10 ab initio models were generated through simulated annealing by GASBOR (*51*) and averaged by DAMAVER (*52*). The resultant low-resolution molecular envelope of each sample was represented in PyMOL by setting the van der Waals distance (vdw) to 5.0 Å and the solvent radius (solvent_radius) to 4.5 Å.

Native electrospray ionization and IMMS

$FimG_{Nte}H$ variant complexes in 15 mM MES (pH 5.6) and 50 mM NaCl were diluted to 10 to 20 µM protein concentration and underwent multiple rounds of buffer exchange through dilution and concentration into 100 mM ammonium acetate (pH 6.5) (>99.99% trace metals basis) such that the final salt concentration was reduced to lower than 10 to 20 µM for clean native electrospray ionization (nESI) spectra. $FimG_{Nte}H$:4Z269 complexes were prepared in the same manner after $FimG_{Nte}H$ variants were incubated with 4Z269 at a 1:1 molar ratio. Samples were loaded at 5 to 10 µl in custom-made electrospray capillaries and injected into a hybrid ion mobility quadrupole time-of-flight mass spectrometer (SYNAPT G2 High Definition Mass Spectrometry, Waters). The instrument was operated under gentle ESI conditions (capillary voltage, 1.5 to 2.2 kV; sampling cone, 2 V; extraction cone, 1 V; source temperature, 36°C). CE was varied to observe dissociation events between $FimG_{Nte}$, FimH, and 4Z269. The pressure of the vacuum/backing region was 5.1 to 5.6 mbar. For the ion mobility measurements, the helium gas flow to the collision cell was 70 ml/min, the ion-mobility spectrometry (IMS) gas flow was 35 ml/min, the IMS wave velocity was 500 m/s, and the IMS wave height was 20 V. Nitrogen was used as the mobility carrier gas. The instrument was externally calibrated up to 8000 mass/charge ratio (m/z) with the clusters produced by ESI of NaI solution (100 mg/ml). The peak picking and data processing were achieved by using MassLynx (version 4.1) and DriftScope software (Waters). The CCSs for protein ions were converted using previously published calibration protocols and databases (*53*). $FimG_{Nte}H$ variants in the presence or absence of 4Z269 were aerosolized by nESI, and native mass spectra were acquired under a range of CEs (5 to 40 V). Each spectrum was acquired every 1 s for 2 min and gated at m/z values of 3054 to 3056 (apo) and 3094 to 3096 (+4Z269) for the +10 charge state. These spectra indicated that all FimH variants entered the gas phase as an intact $FimG_{Nte}H$ complex at low CE but steadily dissociated with increasing CE (fig. S3A). These spectra also revealed that $FimG_{Nte}H$ variants stably associated with 4Z269 in accordance with the relative binding strengths of the FimH alleles: 4Z269 occupies ~100% of A27V/V163A, ~90% of WT, ~50% of A62S, and ~0% of Q133K (fig. S3B). The +10 charge state corresponding to intact $FimG_{Nte}H$ variants was then subjected to ion mobility analysis at various CEs. CCS distributions were modeled as a sum of two Gaussian curves because modeling by one Gaussian curve resulted in significantly poorer fits in nearly all cases (table S2).

Protein crystallization and structure determination

Crystals of $FimG_{Nte}H$ A62S grew under numerous polyethylene glycol (PEG) conditions at 20°C by hanging drop vapor diffusion in 96-well plates. The diffracted crystals of $FimG_{Nte}H$ A62S were grown within the PEG II crystallization screen (Qiagen) by mixing 100 nl of protein (7.5 mg/ml) with 100 nl of mother liquor [0.2 M calcium acetate, 0.1 M Hepes (pH 7.5), and 10% PEG 8000] and equilibrated against 75 µl of mother liquor in the reservoir. These crystals took on a thick rectangular prism morphology and were picked directly from the 96-well screen. They were transferred into a cryoprotectant [0.2 M calcium acetate, 0.1 M MES (pH 5.6), 25% PEG 8000, and 20% glycerol] and then flash-frozen in a cryostream. Crystals of $FimG_{Nte}H$ A27V/V163A were grown at 20°C by hanging drop vapor diffusion by mixing 1 µl of protein (5 mg/ml) with 1 µl of mother liquor [0.2 M calcium acetate, 0.1 M Hepes (pH 7.5), and 5% PEG 8000] and 0.5 µl of 0.1 M cadmium chloride and equilibrated against 1 ml of mother liquor in wells of a 24-well plate. These crystals took on a thin-plate morphology. They were transferred into a cryoprotectant [0.2 M calcium acetate, 0.1 M Hepes (pH 7.5), 25% PEG 8000, and 20% glycerol] and then flash-frozen in a cryostream. Diffraction data were collected at 100 K at an in-house facility equipped with a rotating anode (Rigaku MicroMax-007 generator), a Rayonix marmux x-ray source, and a Mar345 image plate detector. Data were indexed and integrated in iMosflm (*54*) and scaled by Scala (*55*). The phase problem was solved by MR using Phaser-MR in Phenix (*56*) with two distinct search ensembles: (i) $FimH_{PD}$ (from PDB ID 1KLF) and $FimH_{LD}$ in the **T** state (from PDB ID 3JWN) as separate domains and (ii) $FimH_{PD}$ (from PDB ID 1KLF) and $FimH_{LD}$ in the **R** state (from PDB ID 1KLF) as separate domains. The best solutions were identified

as a **T** conformation for $FimG_{Nte}H$ A62S and a **bent R** conformation (90° between $FimH_{LD}$ and $FimH_{PD}$) for $FimG_{Nte}H$ A27V/V163A. Several rounds of refinements were performed in phenix.refine to improve the final models.

Molecular dynamics

Crystal structures of $FimG_{Nte}H$ published in this study along with models of $FimG_{Nte}H$ based on previous crystal structures (G_{Nte} docked on H from CH structure) in the absence or presence of ligands were used to initiate MD simulations. Structural models of $FimG_{Nte}H$ variants were created with the in silico mutagenesis wizard in PyMOL after the mutant side-chain rotamer with the fewest steric clashes was selected. Structural models were then prepared within the CHARMM36 force field and the TIP3P water model by the MD software package GROMACS-4.6.7 (*57*). The system was first solvated in a cubic box, with sides equal to 130 Å in the presence of 50 mM NaCl. The structure was then energy-minimized to reduce steric clashes, and the system was finally equilibrated at constant temperature (37°C) and pressure (1 atm). Conventional unrestrained MD simulations were then performed with steps of 2 fs for a total time of ~15 to 20 ns for each run, collecting four replicates for simulations on the **T** (5JQI), **bent R** (5JR4), and **elongated R** (based on 1KLF) conformations for WT FimH. Longer simulations were also performed at 100 to 200 ns for three replicates for all FimH variants in these conformations with similar results. Coordinates were saved every 0.1 ns. Commands in GROMACS and graphical output in MATLAB were used to analyze simulation trajectories.

Conformational phase space

Conformational phase space calculations were performed with custom in-house scripts in PyMOL and MATLAB after alignment of the pilin domain to a reference structure ($FimH_{PD}$ from FimCH). The coordinates of the following atoms were tracked and assigned the corresponding labels: Leu225 and CD2 (pip1 for "point in pilin 1"), Leu193 and CD1 (pip2), Ala247 and N (pip3), Leu193 and CA (pip4), Leu129 and CD2 (pil1 for "point in lectin 1"), Val20 and CG1 (pil2), and Val105 and N (pil3). The points {pip1, pip2} and {pip2, pil1} define vectors along the longest dimension of $FimH_{PD}$ and $FimH_{LD}$, respectively. The points {pip2, pip3, pip4} and {pil1, pil2, pil3} define transverse planes that respectively bisect $FimH_{PD}$ and $FimH_{LD}$ perpendicular to the axis of the longest dimension. Bend angle is defined as the {pip1, pip2, pil1} angle. Twist angle is defined as the {pip1, pip2, *x*} angle, where *x* is defined as the point on the {pil1, pil2, pil3} plane at a fixed radial distance from pil1 that is closest to the {pip2, pip3, pip4} plane. Orientation angle is defined as the {pip3, pip2, *y*} angle, where *y* is the point on the {pip2, pip3, pip4} plane closest to *x*. These angles are schematically represented in fig. S5A.

Mouse infections

For the uncomplicated UTI model, 7- to 8-week-old female C3H/HeN mice were obtained from Envigo. Mice were anesthetized and inoculated via transurethral catheterization with 50 µl of bacterial suspension (~1×10^7 to 2×10^7 CFU in total) in PBS. At times indicated, mice were sacrificed, and bladders were aseptically removed and processed for CFU determination (*37*). For the CAUTI model, a 5-mm piece of silicon tubing (RenaSil 0.635-mm outer diameter) was inserted transurethrally into the bladders of 6-week-old female C57BL/6 mice, as previously described (*37*). Twenty-four hours after implantation, the mice were transurethrally infected with ~2×10^7 CFU of UTI89 expressing either the WT or A27V/V163A allele of FimH with the *fim* operon locked in the phase on state (*13*). Mice were sacrificed 24 or 72 hpi, and bacteria colonizing the bladder and implant were plated for quantification.

Bladder epithelial cell studies

Human bladder epithelial cells, designated 5637 (ATCC HTB-9) cells, were obtained from the American Type Culture Collection and maintained in RPMI 1640 supplemented with heat-inactivated 10% (v/v) fetal bovine serum at 37°C in the presence of 5% CO_2. Confluent, serum-starved 5637 cells in 24-well plates were infected with UTI89 strains at a multiplicity of infection of 10. After 30 min, culture media were replaced either by fresh culture media or by media with gentamicin sulfate (120 µg/ml) (Sigma-Aldrich) to kill extracellular bacteria. Cells were further incubated for 1 hour, washed rigorously, solubilized with 1% Triton X-100, quenched with PBS, and plated for bacterial CFU quantification.

SUPPLEMENTARY MATERIALS

Supplementary material for this article is available at http://advances.sciencemag.org/cgi/content/full/3/2/e1601944/DC1

fig. S1. Structural analysis of solved $FimG_{Nte}H$ complex crystal structures.
fig. S2. Structural comparison of all known FimH conformations.
fig. S3. Solution analysis of FimCH and $FimG_{Nte}H$ variants.
fig. S4. Native and ion mobility mass spectra of $FimG_{Nte}H$ variants in the absence or presence of 4Z269.
fig. S5. Conformational dynamics and binding mechanisms of $FimG_{Nte}H$ WT.
table S1. Data collection and refinement statistics.
table S2. Fitted parameter values and analysis of Gaussian peaks on CCS distributions.
movie S1. Combined MD simulation trajectories initiated from the **T** state in the absence of mannose.
movie S2. Combined MD simulation trajectories initiated from the **bent R** state in the absence of mannose.
movie S3. Combined MD simulation trajectories initiated from the **elongated R** state in the absence of mannose.
movie S4. Combined MD simulation trajectories initiated from the **T** state in the presence of mannose.
movie S5. Combined MD simulation trajectories initiated from the **bent R** state in the presence of mannose.
movie S6. Combined MD simulation trajectories initiated from the **elongated R** state in the presence of mannose.
movie S7. Combined MD simulation trajectories initiated from the **T** state in the presence of oligomannose-3.
movie S8. Combined MD simulation trajectories initiated from the **bent R** state in the presence of oligomannose-3.

REFERENCES AND NOTES

1. M. A. Croxen, B. B. Finlay, Molecular mechanisms of *Escherichia coli* pathogenicity. *Nat. Rev. Microbiol.* **8**, 26–38 (2010).
2. D. A. Rasko, V. Sperandio, Anti-virulence strategies to combat bacteria-mediated disease. *Nat. Rev. Drug Discov.* **9**, 117–128 (2010).
3. A. Persat, C. D. Nadell, M. K. Kim, F. Ingremeau, A. Siryaporn, K. Drescher, N. S. Wingreen, B. L. Bassler, Z. Gitai, H. A. Stone, The mechanical world of bacteria. *Cell* **161**, 988–997 (2015).
4. K. A. Kline, S. Fälker, S. Dahlberg, S. Normark, B. Henriques-Normark, Bacterial adhesins in host-microbe interactions. *Cell Host Microbe* **5**, 580–592 (2009).
5. H.-C. Flemming, J. Wingender, U. Szewzyk, P. Steinberg, S. A. Rice, S. Kjelleberg, Biofilms: An emergent form of bacterial life. *Nat. Rev. Microbiol.* **14**, 563–575 (2016).
6. A. R. Ronald, L. E. Nicolle, E. Stamm, J. Krieger, J. Warren, A. Schaeffer, K. G. Naber, T. M. Hooton, J. Johnson, S. Chambers, V. Andriole, Urinary tract infection in adults: Research priorities and strategies. *Int. J. Antimicrob. Agents* **17**, 343–348 (2001).
7. G. Waksman, S. J. Hultgren, Structural biology of the chaperone-usher pathway of pilus biogenesis. *Nat. Rev. Microbiol.* **7**, 765–774 (2009).
8. M. A. Mulvey, Y. S. Lopez-Boado, C. L. Wilson, R. Roth, W. C. Parks, J. Heuser, S. J. Hultgren, Induction and evasion of host defenses by type 1-piliated uropathogenic *Escherichia coli*. *Science* **282**, 1494–1497 (1998).

9. G. G. Anderson, J. J. Palermo, J. D. Schilling, R. Roth, J. Heuser, S. J. Hultgren, Intracellular bacterial biofilm-like pods in urinary tract infections. *Science* **301**, 105–107 (2003).
10. S. S. Justice, C. Hung, J. A. Theriot, D. A. Fletcher, G. G. Anderson, M. J. Footer, S. J. Hultgren, Differentiation and developmental pathways of uropathogenic *Escherichia coli* in urinary tract pathogenesis. *Proc. Natl. Acad. Sci. U.S.A.* **101**, 1333–1338 (2004).
11. D. A. Rosen, T. M. Hooton, W. E. Stamm, P. A. Humphrey, S. J. Hultgren, Detection of intracellular bacterial communities in human urinary tract infection. *PLOS Med.* **4**, e329 (2007).
12. L. Robino, P. Scavone, L. Araujo, G. Algorta, P. Zunino, M. C. Pírez, R. Vignoli, Intracellular bacteria in the pathogenesis of *Escherichia coli* urinary tract infection in children. *Clin. Infect. Dis.* **59**, e158–e164 (2014).
13. S. L. Chen, C. S. Hung, J. S. Pinkner, J. N. Walker, C. K. Cusumano, Z. Li, J. Bouckaert, J. I. Gordon, S. J. Hultgren, Positive selection identifies an in vivo role for FimH during urinary tract infection in addition to mannose binding. *Proc. Natl. Acad. Sci. U.S.A.* **106**, 22439–22444 (2009).
14. D. J. Schwartz, V. Kalas, J. S. Pinkner, S. L. Chen, C. N. Spaulding, K. W. Dodson, S. J. Hultgren, Positively selected FimH residues enhance virulence during urinary tract infection by altering FimH conformation. *Proc. Natl. Acad. Sci. U.S.A.* **110**, 15530–15537 (2013).
15. D. Choudhury, A. Thompson, V. Stojanoff, S. Langermann, J. Pinkner, S. J. Hultgren, S. D. Knight, X-ray structure of the FimC-FimH chaperone-adhesin complex from uropathogenic *Escherichia coli*. *Science* **285**, 1061–1066 (1999).
16. C.-S. Hung, J. Bouckaert, D. Hung, J. Pinkner, C. Widberg, A. DeFusco, C. G. Auguste, R. Strouse, S. Langermann, G. Waksman, S. J. Hultgren, Structural basis of tropism of *Escherichia coli* to the bladder during urinary tract infection. *Mol. Microbiol.* **44**, 903–915 (2002).
17. I. Le Trong, P. Aprikian, B. A. Kidd, M. Forero-Shelton, V. Tchesnokova, P. Rajagopal, V. Rodriguez, G. Interlandi, R. Klevit, V. Vogel, R. E. Stenkamp, E. V. Sokurenko, W. E. Thomas, Structural basis for mechanical force regulation of the adhesin FimH via finger trap-like β sheet twisting. *Cell* **141**, 645–655 (2010).
18. G. Phan, H. Remaut, T. Wang, W. J. Allen, K. F. Pirker, A. Lebedev, N. S. Henderson, S. Geibel, E. Volkan, J. Yan, M. B. A. Kunze, J. S. Pinkner, B. Ford, C. W. M. Kay, H. Li, S. J. Hultgren, D. G. Thanassi, G. Waksman, Crystal structure of the FimD usher bound to its cognate FimC–FimH substrate. *Nature* **474**, 49–53 (2011).
19. S. Geibel, E. Procko, S. J. Hultgren, D. Baker, G. Waksman, Structural and energetic basis of folded-protein transport by the FimD usher. *Nature* **496**, 243–246 (2013).
20. F. G. Sauer, K. Fütterer, J. S. Pinkner, K. W. Dodson, S. J. Hultgren, G. Waksman, Structural basis of chaperone function and pilus biogenesis. *Science* **285**, 1058–1061 (1999).
21. C. H. Jones, J. S. Pinkner, R. Roth, J. Heuser, A. V. Nicholes, S. N. Abraham, S. J. Hultgren, FimH adhesin of type 1 pili is assembled into a fibrillar tip structure in the Enterobacteriaceae. *Proc. Natl. Acad. Sci. U.S.A.* **92**, 2081–2085 (1995).
22. F. G. Sauer, J. S. Pinkner, G. Waksman, S. J. Hultgren, Chaperone priming of pilus subunits facilitates a topological transition that drives fiber formation. *Cell* **111**, 543–551 (2002).
23. H. Remaut, R. J. Rose, T. J. Hannan, S. J. Hultgren, S. E. Radford, A. E. Ashcroft, G. Waksman, Donor-strand exchange in chaperone-assisted pilus assembly proceeds through a concerted β strand displacement mechanism. *Mol. Cell* **22**, 831–842 (2006).
24. O. Yakovenko, S. Sharma, M. Forero, V. Tchesnokova, P. Aprikian, B. Kidd, A. Mach, V. Vogel, E. Sokurenko, W. E. Thomas, FimH forms catch bonds that are enhanced by mechanical force due to allosteric regulation. *J. Biol. Chem.* **283**, 11596–11605 (2008).
25. S. L. Chen, C.-S. Hung, J. Xu, C. S. Reigstad, V. Magrini, A. Sabo, D. Blasiar, T. Bieri, R. R. Meyer, P. Ozersky, J. R. Armstrong, R. S. Fulton, J. P. Latreille, J. Spieth, T. M. Hooton, E. R. Mardis, S. J. Hultgren, J. I. Gordon, Identification of genes subject to positive selection in uropathogenic strains of *Escherichia coli*: A comparative genomics approach. *Proc. Natl. Acad. Sci. U.S.A.* **103**, 5977–5982 (2006).
26. M. M. Sauer, R. P. Jakob, J. Eras, S. Baday, D. Eriş, G. Navarra, S. Bernèche, B. Ernst, T. Maier, R. Glockshuber, Catch-bond mechanism of the bacterial adhesin FimH. *Nat. Commun.* **7**, 10738 (2016).
27. C. K. Cusumano, J. S. Pinkner, Z. Han, S. E. Greene, B. A. Ford, J. R. Crowley, J. P. Henderson, J. W. Janetka, S. J. Hultgren, Treatment and prevention of urinary tract infection with orally active FimH inhibitors. *Sci. Transl. Med.* **3**, 109ra115 (2011).
28. D. Schneidman-Duhovny, M. Hammel, A. Sali, FoXS: A web server for rapid computation and fitting of SAXS profiles. *Nucleic Acids Res.* **38**, W540–W544 (2010).
29. J. Bouckaert, J. Mackenzie, J. L. De Paz, B. Chipwaza, D. Choudhury, A. Zavialov, K. Mannerstedt, J. Anderson, D. Piérard, L. Wyns, P. H. Seeberger, S. Oscarson, H. De Greve, S. D. Knight, The affinity of the FimH fimbrial adhesin is receptor-driven and quasi-independent of *Escherichia coli* pathotypes. *Mol. Microbiol.* **61**, 1556–1568 (2006).
30. A. Wellens, C. Garofalo, H. Nguyen, N. Van Gerven, R. Slättegård, J.-P. Hernalsteens, L. Wyns, S. Oscarson, H. De Greve, S. Hultgren, J. Bouckaert, Intervening with urinary tract infections using anti-adhesives based on the crystal structure of the FimH–oligomannose-3 complex. *PLOS ONE* **3**, e2040 (2008).
31. A. Wellens, M. Lahmann, M. Touaibia, J. Vaucher, S. Oscarson, R. Roy, H. Remaut, J. Bouckaert, The tyrosine gate as a potential entropic lever in the receptor-binding site of the bacterial adhesin FimH. *Biochemistry* **51**, 4790–4799 (2012).
32. V. B. Rodriguez, B. A. Kidd, G. Interlandi, V. Tchesnokova, E. V. Sokurenko, W. E. Thomas, Allosteric coupling in the bacterial adhesive protein FimH. *J. Biol. Chem.* **288**, 24128–24139 (2013).
33. J. Fogh, Cultivation, characterization, and identification of human tumor cells with emphasis on kidney, testis, and bladder tumors. *Natl. Cancer Inst. Monogr.* 5–9 (1978).
34. P. S. Guiton, C. S. Hung, L. E. Hancock, M. G. Caparon, S. J. Hultgren, Enterococcal biofilm formation and virulence in an optimized murine model of foreign body-associated urinary tract infections. *Infect. Immun.* **78**, 4166–4175 (2010).
35. C. N. Murphy, M. S. Mortensen, K. A. Krogfelt, S. Clegg, Role of *Klebsiella pneumoniae* type 1 and type 3 fimbriae in colonizing silicone tubes implanted into the bladders of mice as a model of catheter-associated urinary tract infections. *Infect. Immun.* **81**, 3009–3017 (2013).
36. A. L. Flores-Mireles, J. S. Pinkner, M. G. Caparon, S. J. Hultgren, EbpA vaccine antibodies block binding of *Enterococcus faecalis* to fibrinogen to prevent catheter-associated bladder infection in mice. *Sci. Transl. Med.* **6**, 254ra127 (2014).
37. M. S. Conover, A. L. Flores-Mireles, M. E. Hibbing, K. Dodson, S. J. Hultgren, Establishment and characterization of UTI and CAUTI in a mouse model. *J. Vis. Exp.*, e52892 (2015).
38. H. S. Raffi, J. M. Bates, D. J. Flournoy, S. Kumar, Tamm-Horsfall protein facilitates catheter associated urinary tract infection. *BMC Res. Notes* **5**, 532 (2012).
39. J. Monod, J. P. Changeux, F. Jacob, Allosteric proteins and cellular control systems. *J. Mol. Biol.* **6**, 306–329 (1963).
40. D. E. Koshland Jr., G. Némethy, D. Filmer, Comparison of experimental binding data and theoretical models in proteins containing subunits. *Biochemistry* **5**, 365–385 (1966).
41. M. F. Perutz, Stereochemistry of cooperative effects in haemoglobin. *Nature* **228**, 726–739 (1970).
42. Q. Cui, M. Karplus, Allostery and cooperativity revisited. *Protein Sci.* **17**, 1295–1307 (2008).
43. H. N. Motlagh, J. O. Wrabl, J. Li, V. J. Hilser, The ensemble nature of allostery. *Nature* **508**, 331–339 (2014).
44. W. E. Thomas, E. Trintchina, M. Forero, V. Vogel, E. V. Sokurenko, Bacterial adhesion to target cells enhanced by shear force. *Cell* **109**, 913–923 (2002).
45. W. E. Thomas, L. M. Nilsson, M. Forero, E. V. Sokurenko, V. Vogel, Shear-dependent 'stick-and-roll' adhesion of type 1 fimbriated *Escherichia coli*. *Mol. Microbiol.* **53**, 1545–1557 (2004).
46. O. Yakovenko, V. Tchesnokova, E. V. Sokurenko, W. E. Thomas, Inactive conformation enhances binding function in physiological conditions. *Proc. Natl. Acad. Sci. U.S.A.* **112**, 9884–9889 (2015).
47. S. E. Greene, M. E. Hibbing, J. Janetka, S. L. Chen, S. J. Hultgren, Human urine decreases function and expression of type 1 pili in uropathogenic *Escherichia coli*. *MBio* **6**, e00820 (2015).
48. K. N. Dyer, M. Hammel, R. P. Rambo, S. E. Tsutakawa, I. Rodic, S. Classen, J. A. Tainer, G. L. Hura, High-throughput SAXS for the characterization of biomolecules in solution: A practical approach. *Methods Mol. Biol.* **1091**, 245–258 (2014).
49. M. V. Petoukhov, D. Franke, A. V. Shkumatov, G. Tria, A. G. Kikhney, M. Gajda, C. Gorba, H. D. T. Mertens, P. V. Konarev, D. I. Svergun, New developments in the *ATSAS* program package for small-angle scattering data analysis. *J. Appl. Crystallogr.* **45**, 342–350 (2012).
50. G. L. Hura, H. Budworth, K. N. Dyer, R. P. Rambo, M. Hammel, C. T. McMurray, J. A. Tainer, Comprehensive macromolecular conformations mapped by quantitative SAXS analyses. *Nat. Methods* **10**, 453–454 (2013).
51. D. I. Svergun, M. V. Petoukhov, M. H. Koch, Determination of domain structure of proteins from X-ray solution scattering. *Biophys. J.* **80**, 2946–2953 (2001).
52. D. Baker, A. E. Krukowski, D. A. Agard, Uniqueness and the ab initio phase problem in macromolecular crystallography. *Acta Crystallogr. D Biol. Crystallogr.* **49**, 186–192 (1993).
53. I. Michaelevski, N. Kirshenbaum, M. Sharon, T-wave ion mobility-mass spectrometry: Basic experimental procedures for protein complex analysis. *J. Vis. Exp.*, 1985 (2010).
54. T. G. G. Battye, L. Kontogiannis, O. Johnson, H. R. Powell, A. G. Leslie, *iMOSFLM*: A new graphical interface for diffraction-image processing with *MOSFLM*. *Acta Crystallogr. D Biol. Crystallogr.* **67**, 271–281 (2011).
55. M. D. Winn, C. C. Ballard, K. D. Cowtan, E. J. Dodson, P. Emsley, P. R. Evans, R. M. Keegan, E. B. Krissinel, A. G. W. Leslie, A. McCoy, S. J. McNicholas, G. N. Murshudov, N. S. Pannu, E. A. Potterton, H. R. Powell, R. J. Read, A. Vagin, K. S. Wilson, Overview of the *CCP*4 suite and current developments. *Acta Crystallogr. D Biol. Crystallogr.* **67**, 235–242 (2011).
56. P. D. Adams, P. V. Afonine, G. Bunkóczi, V. B. Chen, I. W. Davis, N. Echols, J. J. Headd, L.-W. Hung, G. J. Kapral, R. W. Grosse-Kunstleve, A. J. McCoy, N. W. Moriarty, R. Oeffner, R. J. Read, D. C. Richardson, J. S. Richardson, T. C. Terwilliger, P. H. Zwart, *PHENIX*: A comprehensive Python-based system for macromolecular structure solution. *Acta Crystallogr. D Biol. Crystallogr.* **66**, 213–221 (2010).
57. H. J. C. Berendsen, D. van der Spoel, R. van Drunen, GROMACS: A message-passing parallel molecular-dynamics implementation. *Comput. Phys. Commun.* **91**, 43–56 (1995).

Acknowledgments: We thank members of the S.J.H. laboratory, C. Frieden, and J. Cooper for helpful suggestions. We also thank R. Stegeman for technical assistance in x-ray data collection, Z. Han for synthesizing and providing 4Z269, and G. Hura and J. Tainer at the Advanced Light Source for SAXS data collection and processing. **Funding:** S.J.H. was supported by NIH National Institute of Allergy and Infectious Diseases (NIAID) grants R01 AI029549, R01 AI048689, and U01 AI095542 and National Institute of Diabetes and Digestive and Kidney Diseases grant R01 DK051406. V.K. was supported by the Medical Scientist Training Program through NIH training grant T32 GM07200. T.J.H. was supported by NIH NIAID grant U01 AI095542. M.L.G. was supported by NIH National Institute for General Medical Sciences (NIGMS) grant P41GM103422. R.V.P. was funded by NIH NIGMS grant P41GM103422. **Author contributions:** V.K., N.H.T., M.L.G., R.V.P., J.J., and S.J.H. designed the research plan. V.K. and J.S.P. purified the proteins. V.K. performed x-ray crystallography, SAXS, ELISA, and in vitro bladder binding and invasion experiments. V.K. and H.Z. performed the IMMS experiments. V.K. and A.S.H. performed the simulations. T.J.H. and M.E.H. performed the animal experiments. V.K., T.J.H., M.E.H., and S.J.H. analyzed and interpreted all data. V.K., \K.W.D., and S.J.H. wrote the manuscript. **Competing interests:** S.J.H., J.J., and T.J.H. have ownership interest in Fimbrion Therapeutics Inc. and may benefit if the company is successful in marketing the mannosides that are related to this research. S.J.H. and J.J. are cofounders, stockholders, and board members of Fimbrion Therapeutics Inc., and T.J.H. is an employee of the same organization with stock options. J.J. has three patents related to the compounds described in the work: U.S. Patent US8937167, "Compounds and methods for treating bacterial infections, " J.J., S.J.H., Z. Han, J. Pinkner, C. Cusumano (Washington University School of Medicine), 20 January 2015; PCT Application WO2012109263, "Mannoside compounds and methods of use thereof," J.J., S.J.H., Z. Han, J. Pinkner, C. Cusumano (Washington University School of Medicine), 16 August 2012; and U.S. Application US20120309701, "Compounds and methods useful for treating bacterial infections," J.J., S.J.H., Z. Han, J. Pinkner, C. Cusumano (Washington University School of Medicine), 6 December 2012. **Data and materials availability:** All data needed to evaluate the conclusions in the paper are present in the paper and/or the Supplementary Materials. Additional data related to this paper may be requested from the authors. The atomic coordinates and structure factors have been deposited in the PDB under accession codes 5JQI and 5JR4.

Submitted 16 August 2016
Accepted 25 January 2017
Published 10 February 2017
10.1126/sciadv.1601944

Citation: V. Kalas, J. S. Pinkner, T. J. Hannan, M. E. Hibbing, K. W. Dodson, A. S. Holehouse, H. Zhang, N. H. Tolia, M. L. Gross, R. V. Pappu, J. Janetka, S. J. Hultgren, Evolutionary fine-tuning of conformational ensembles in FimH during host-pathogen interactions. *Sci. Adv.* **3**, e1601944 (2017).

ScienceAdvances
AAAS

Evolutionary fine-tuning of conformational ensembles in FimH during host-pathogen interactions

Vasilios Kalas, Jerome S. Pinkner, Thomas J. Hannan, Michael E. Hibbing, Karen W. Dodson, Alex S. Holehouse, Hao Zhang, Niraj H. Tolia, Michael L. Gross, Rohit V. Pappu, James Janetka and Scott J. Hultgren (February 10, 2017)
Sci Adv 2017, 3:.
doi: 10.1126/sciadv.1601944